A Comprehensive Monte Carlo Study of Out-Of-Field Secondary Neutron Spectra in a Scanned-Beam Proton Therapy Gantry Room

F S Englbrecht[1], S Trinkl[2,3], V Mares[2], W Rühm[2], M. Wielunski[2], J J Wilkens[3,5], M Hillbrand[4] and K Parodi*[1]

[1] LMU Munich, Faculty of Physics, Department of Medical Physics, Munich, Germany
[2] Helmholtz Zentrum München, Institute of Radiation Protection, Neuherberg, Germany
[3] Technical University of Munich, Physics Department, Garching, Germany
[4] Rinecker Proton Therapy Center, Munich, Germany
[5] Technical University of Munich, Department of Radiation Oncology, School of Medicine and Klinikum rechts der Isar, Munich, Germany

Version typeset October 13, 2020

*Author to whom correspondence should be addressed. email: franz.englbrecht@lmu.de

Abstract

Purpose: To simulate secondary neutron radiation fields that had been measured at different relative positions during phantom irradiation inside a scanning proton therapy gantry treatment room. Further, to identify origin, energy distribution, and angular emission of the secondary neutrons as a function of proton beam energy.

Methods: The FLUKA Monte Carlo code was used to model the relevant parts of the treatment room in a scanned pencil beam proton therapy gantry including shielding walls, floor, major metallic gantry-components, patient table, and a homogeneous PMMA target. The proton beams were modeled based on experimental beam ranges in water and spot shapes in air. Neutron energy spectra were simulated at 0°, 45°, 90° and 135° relative to the beam axis at 2 m distance from isocenter, monoenergetic $11 \times 11\,\mathrm{cm}^2$ fields from 200 MeV, 140 MeV, 75 MeV initial proton beams, as well as for 118 MeV protons with a 5 cm thick PMMA range shifter. The total neutron spectra were scored for these four positions and proton energies. FLUKA neutron spectra simulations were crosschecked with Geant4 simulations using initial proton beam properties from FLUKA-generated phase spaces. Additionally, the room-components generating secondary neutrons in the room and their contributions to the total spectrum were identified and quantified.
Results: FLUKA and Geant4 simulated neutron spectra showed good general agreement with published measurements in the whole simulated neutron energy range of 10^{-10} to 10^{3} MeV. As in previous studies, high-energy (E $\geq$ 19.6 MeV) neutrons from the phantom are most prevalent along 0°, while thermalized (1 meV $\leq$ E $<$ 0.4 eV) and fast (100 keV $\leq$ E $<$ 19.4 MeV) neutrons dominate the spectra in the lateral and

backscatter direction. The iron of the large bending magnet and its counterweight mounted on the gantry were identified as the most determinant sources of secondary fast-neutrons, which have been lacking in simplified room simulations.

Conclusions: The results helped disentangle the origin of secondary neutrons and their dominant contributions and were strengthened by the fact that a cross comparison was made using two independent Monte Carlo codes. The complexity of such room model can in future limited using the result. They may further be generalized in that they can be used for an assessment of neutron fields, possibly even at facilities where detailed neutron measurements and simulations cannot be performed. They may also help to design future proton therapy facilities and to reduce unwanted radiation doses from secondary neutrons to patients.

I. Introduction

It has been suggested that proton therapy could enable better tumor control probabilities and demonstrated to do so in treatment of cancers of the central nervous system, for head and neck cancers, and tumors inside the eye[1]. Recently, data from ion therapy irradiation of prostate cancer suggesting lower risk of subsequent secondary cancer for ion therapy have been reported[2]. Compared with conventional radiation treatments employing photons, proton beam therapy enables to spatially confine the therapeutic radiation dose to the targeted tumor volume and reduce the integral out-of-field dose to healthy tissue.

Although most of the kinetic energy of a clinical proton beam is deposited in tissue via electromagnetic interactions with atomic electrons[3], proton induced nuclear reactions can generate unwanted secondary radiation like stray neutrons within the beam line elements, the structures of the gantry room, and even within the patients themselves[4,5]. Although the stray neutron dose is much lower in magnitude compared to the therapeutic proton dose, it penetrates the whole body of the patient and can be up to 20-times more biologically effective[6]. Unwanted neutrons, especially relevant for pediatric or re-irradiation patients, can deposit their kinetic energy inside the patient far outside the desired treatment volume and increase the risk of secondary cancer [4,7,8]. Although neutron contribution is typically neglected in current treatment planning systems, there are efforts ongoing to integrate the information of risk estimation in the planning process, which will require also the room model[9,10].

In order to make quantitative assessments in calculating the prompt dose rates for shielding design of treatment rooms, the systematic knowledge of the neutron spectrum is essential. These spectra are used to calculate effective doses for a given incident neutron field by applying *fluence to effective dose* conversion coefficients that vary with neutron energy[11]. In the context of radiation protection, it has been reported that the radiation quality factor w_R of neutrons is largest for epithermal, fast and high-energy neutrons in the interval 10 keV to 10^2 MeV, which is a 10-times increased w_R compared to $w_R = 2 - 3$ elsewhere (Fig. 1) or $w_R = 1$ for photon radiation[6,11]. Moreover, these quality factors, although conceived for radioprotection purposes, have been already used as a reasonable approximation for the estimation of biological effectiveness for organ equivalent dose calculations in proton therapy, e.g., Rechner et al. and Zheng et al.[10,12].

Like the system used in this study, most modern active spot scanning proton therapy systems employ an isochronous cyclotron with a fixed extraction energy of $230 - 250\,\mathrm{MeV}$ and an energy degrading system several meters upstream of the treatment nozzle[13,14]. By placing this strongest source of secondary neutrons in a separately shielded area (the energy degrader), actively scanned proton therapy has been reported to reduce the secondary neutron ambient dose exposure to patients by up to one order of magnitude in comparison to delivery techniques based on passive scattering devices placed in the treatment nozzle for beam shaping[15,16,17].

Detailed room models were used in Monte Carlo simulations to study the out-of-field dose and optimization of the treatment room design[18,19,20]. To a lesser extent and mostly modeling passively scattered proton beam facilities, the spectra and number of secondary neutrons were studied[16,21,22,23]. The studies used models of the gantry and treatment room, but the mostly vague description of used materials and the treatment field specific collimators and compensators have so far hindered generalizing the results. Recently, literature is starting to provide more detailed simulation models and spectra studies coupled to measurements for the Mevion S250 gentry-mounted passively scattered proton system[24,25,26].

Because active beam scanning has begun to replace passive beam delivery techniques, and literature on secondary neutrons from active treatment facilities is still sparse, we performed a detailed Monte Carlo analysis for monoenergetic treatment fields in order to enable comparative studies of the contributions of the gantry and room elements on the secondary neutron generation[18,27,28,29]. We expect spot scanning facilities to be more uniform in design and the present neutron spectra to be better intercomparable, because the spot scanning technique does not place field-specific material into the beam path[30]. In this case, the patient will therefore be the main source of secondary neutrons and a detailed study of the spot scanning room and gantry elements is desirable[31,32,33]. Of the modeled Varian ProBeam® therapy system, 17 rooms were in operation and 20 were under construction in 2019[34,35].

Although the purpose of the previously published studies on ambient dose equivalent from neutrons did not include the detailed validation of the Monte Carlo (MC) simulation models of the respective treatment facilities, the obtained measurement and simulation data showed that large differences may occur[17,20]. For a scattering facility which causes neutrons to be mostly generated in the passive beam modulators and field shaping apartures and

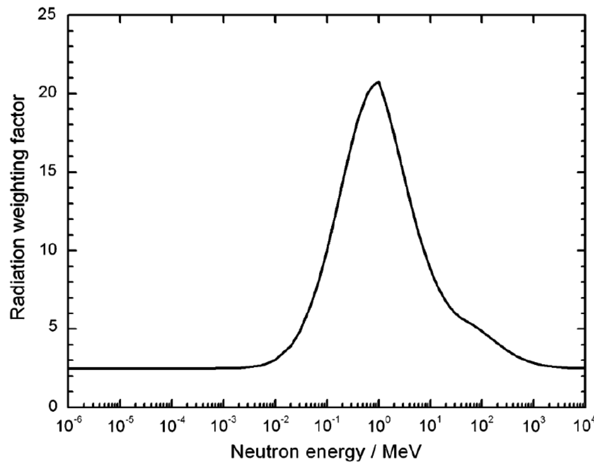

Figure 1: Radiation weighting factor w_R used in radiological protection[11].

not in the room itself, Farah et al. already reported that elements as the bending magnet and mechanical gantry structure should be adjusted to minimize such discrepancies between measurement and simulation[20]. For the measurements underlying the presented simulation study, the authors chose a physically accessible quantity, the energy resolved neutron fluence $\phi(E)$, which will be abbreviated as *neutron spectrum* in this article. Nuclear reaction cross sections needed for MC simulations are strongly dependent on neutron energy as is the simulated secondary radiation field[36,37]. With monoenergetic proton fields, this facilitated a quantitative and objective evaluation of the secondary neutron spectra as well as the dependence on the proton beam energy and the specific setting of the treatment room geometry. Monoenergetic proton fields were chosen in the measurement campaign in order to distinguish the influence of proton beam energy, as well as the influence of the individual treatment room components and the phantom itself on the secondary radiation field. In fact, nuclear reaction channels become enabled energetically when the neutron energy changes due to scattering or resonances of neutron production in materials influencing the field of secondary particles. Previous studies reported differences of a factor of 2-4 in ambient dose equivalent, also originating from approximations in the beamline and room modeling[28,38]. In order to investigate the reasons for such differences, the influence of room components on the neutron spectra measured by Trinkl et al. was simulated systematically.

The report is divided into two main simulation campaigns. First, the FLUKA MC code was used to reproduce published neutron spectra measured by our team at the clinical Varian ProBeam® pencil beam scanning facility[39,40]. Simulated FLUKA spectra were cross-checked using Geant4 MC simulations using FLUKA generated phase spaces as input[41]. In a second step, the validated FLUKA room model was also used to study the contributions of the modeled treatment room elements and concrete shielding to the full neutron spectrum.

II. Methods

II.A. Previously measured secondary neutron spectra

Neutron spectra had been measured using an extended-range Bonner sphere spectrometer (ERBSS) inside a gantry treatment room at the Rinecker Proton Therapy Center (RPTC) in Munich, Germany[37]. RPTC uses a Varian ProBeam® nozzle for pencil beam spot scanning delivery[14,42]. The ERBSS uses ^{3}He spherical proportional counters placed inside of polyethylene spheres of different radii (some of them with lead shells) in order to reliably measure neutron spectra in the energy range from thermal up to high-energy neutrons[32]. The Bonner spheres had been placed at 0°, 45°, 90° and 135° at 2 m distance from the isocenter, relative to the incident direction of the proton beam, in a horizontal plane (See figs. 1a, 1b of the supplementary material[43] for a photograph and a drawing of the measurement setup). Monoenergetic irradiation fields of $11 \times 11\,\mathrm{cm}^2$ lateral size at initial beam energies of 200 MeV, 140 MeV, 118 MeV and 75 MeV had been delivered to a PMMA slab phantom (30 cm × 30 cm × 30 cm). The 118 MeV field was irradiated using a 5 cm PMMA range shifter to generate the same proton beam range in water as a 75 MeV beam. For each energy, we had unfolded neutron spectra for the four angular positions in the possible range of 10^{-9} MeV to 10^{4} MeV[37] using 10 log-equidistant intervals per decade.

The results showed a strong dependence of the secondary neutron field on the angular measurement position and proton beam energy. Comparison of the neutron spectra from simple bare phantom simulations without room model, which had been used as input for the ERBSS unfolding, to the measurement results showed considerable differences. The differences were especially notable in interval of increased biological effectiveness (Fig. 1). It was evident that the influence of the treatment room dominates the characteristics of the secondary neutron field (See Fig. 3 and Fig. 4 by Trinkl et al.[37]). In order to clarify the origin of the secondary neutrons and systematically understand the room influence on the different components of the neutron spectrum, we modeled the RPTC treatment room and re-simulated the experiments.

II.B. FLUKA beam model

We used the FLUKA Monte Carlo code to perform the treatment room simulations because the code has been extensively used in shielding calculations, radiation protection and dosimetry[39,44]. A detailed FLUKA model of the RPTC nozzle[45] was previously benchmarked against measured depth-dose distributions in water and lateral spot shape measurements in air with sub-mm accuracy. The model in this study was extended by the shielding walls and room components (see section II.E.), instead of simply using an idealistic proton beam model based on estimates of proton beam energy, energy spread, and spot shape.

II.C. Detailed treatment room model

In contrast to a previous Monte Carlo study by Hofmann et al. modeling the cyclotron and energy selection system area of the facility[46], we modeled the inside of a clinical gantry room (Fig. 2) employing the modern proton pencil beam spot scanning technique. In addition to the literature, information was also provided by the local medical physics department[13,14,45].

Two meter thick walls, enclosing the treatment room $(11 \times 11 \times 20\,\mathrm{m}^3)$ and made of standard concrete from the FLUKA material database, formed the outer mantle (Fig. 2 bottom). Standard air was used to fill the shelter. The entrance maze included the concrete floor. The gantry was split into two main model components: a gantry wheel and gantry cone. The section of the floor accommodating the patient support device and table was included as a 1 cm plate of standard iron in FLUKA and extends 130 cm cm into the inner gantry wheel. The wheel consists of two concentric 2 cm thick iron cylinder shells of 5.08 m radius (inner shell) and 6 m radius (outer shell) (See Fig. 2 top). The size of the gantry cone matched the installed, cone shaped, complex back support structure of the gantry. For simplification, the cone model reproduces just the outer dimension and no internal structure. It was modeled as solid iron of reduced density $\rho_{cone} = 2\,\mathrm{g/cm}^3$ in order to reproduce the actual weight[14]. The bending magnet of the gantry was included as a massive cube of iron. On the opposite site of the outer gantry wheel, the counterweight of the bending magnet was modeled based on the exact geometrical drawing by the manufacturer. The geometry of the counterweight was used to calculate a mass of 18.7 tons of massive iron when using $\rho_{Fe} = 7.874\,\mathrm{g/cm}^3$. The counterweight edge length was hence set to 133 cm to match the bending magnet mass.

The primary protons were sampled inside a small vacuum region 3 cm upstream of the vacuum window and the beam monitor chambers using the previously published nozzle model[45]. After 86 cm downstream, the protons and generated secondary particles hit the front surface of a PMMA phantom, consistent with the phantom position as used for the ERBSS measurements[37]. The density of the slab phantom at the isocenter, made of PMMA, was the default value as used by the local medical physics staff for quality assurance procedures. The value of ($\rho_{PMMA} = 1.2\,\mathrm{g/cm^3}$) was dosimetrically verified previously.

II.D. Simulation settings

FLUKA uses a multi-group technique for neutron transport in the energy range where neutron cross section tables are used (typically for $E \leq 20\,\mathrm{MeV}$). In the multi-group approach, 260 energy groups are used in the simulation of the elastic and inelastic interactions of neutrons[47]. The total energy spectra of secondary neutrons were obtained using FLUKA multichannel (260 fixed bins in the interval $10^{-9}\,\mathrm{MeV}$ to 20 MeV, log-equidistant above 20 MeV) detectors called 'USRTRACK' scorers.

Four of these spherical 'USRTRACK' detectors of 10 cm radius were placed around the phantom isocenter in the reported ERBSS measurement positions[37]. Because multi-scattering of secondary neutrons down to thermalization is CPU-time consuming, we simulated 3.5×10^9 primary protons for each of the four primary proton beam energies to acquire reasonable statistics in the fixed spectral neutron binning. All simulations used FLUKA Version 2c.3 with settings 'HADROTHErapy'.

Secondly, the FLUKA user routine *fluscw.f* was used to filter during runtime the 'USRTRACK' spectra, depending on the room element in which a scored secondary neutron had been generated. The neutron origin was accessed using the USDRAW section of the mgdraw.f user routine, which automatically is called at runtime after inelastic interactions. The region of neutron origin was saved in ISPUSR variables during the production reactions occurring, like $X(p, xn)Y$, $X(n, xn)Y$ or $X(\gamma, xn)Y$. The information on the neutron origin was propagated through the simulation of each neutron trajectory and used for filtering when the neutron entered one of the four detector positions. The individually considered regions of neutron origin were:

- The bending magnet
- The iron counterweight
- The PMMA phantom
- The two gantry cylinders
- The concrete floor of the maze
- The iron plate ranging into the gantry
- The outer concrete walls enclosing the shelter
- The gantry iron cone of reduced density.

Because the quality of the nuclear models in MC codes is energy dependent, we graphically analyzed the four proton beam energies over the full neutron energy range. For a quantitative evaluation, the neutron spectra subsequently were further binned into four neutron energy intervals, similar to those of the ERBSS data[37]: Thermal ($1\,\text{meV} \leq \text{E} < 0.4\,\text{eV}$), epithermal ($0.4\,\text{eV} \leq \text{E} < 100\,\text{keV}$), fast ($100\,\text{keV} \leq \text{E} < 19.4\,\text{MeV}$) and high-energy ($\text{E} \geq 19.6\,\text{MeV}$) (Tables 1).

II.E. Crosscheck of FLUKA results with Geant4 using FLUKA phase space

Although the FLUKA Monte Carlo code is known to provide accurately benchmarked results in the employed energy range, we used the Geant4 general purpose Monte Carlo code[41] to verify the FLUKA simulation results of our room model. Geant4 was also previously employed in the calculation of particle transport problems and the simulation of secondary neutron spectra[48,49].

For the four energies 200 MeV, 140 MeV, 118 MeV and 75 MeV, we generated particle phase space files using the FLUKA user routine mgdraw.f in order to avoid a full remodeling of the nozzle and beam parameters in Geant4. The phase space files were scored at the exit of the treatment nozzle downstream from all beam monitors and the vacuum window and reported on a single particle level: *Particle type, kinetic energy, X- and Y- positions and direction vector*. Geant4 was used with the same physics list as used for previously reported simulations of secondary neutron spectra (QGSP_BIC_HP with G4StandardEMPhysics_option3 and G4NeutronHPThermalScattering)[37,50]. We set up the same treatment room in Geant4 excluding the nozzle model.

Normalization of the simulation results to absolute dose per treatment Gray for both FLUKA and Geant4 results was obtained by using the established monitor unit to absolute dose relationship established for the nozzle model by Würl et al[45]. The normalized spectra were compared to the spectra from Trinkl et al., who normalized their spectra to the nominal planned Bragg peak dose as reported by the treatment planning system.

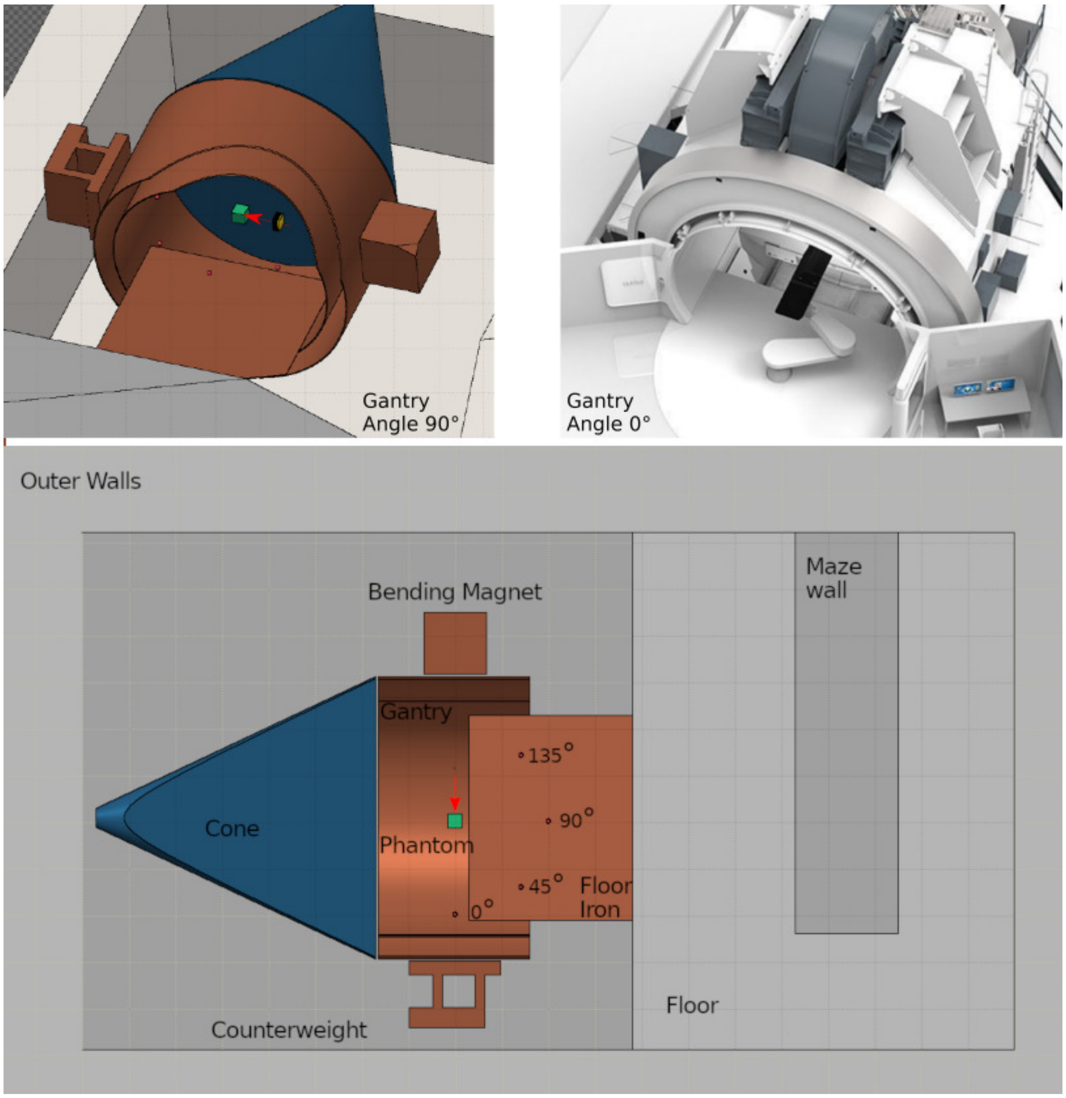

Figure 2: *Top:* 3D FLUKA model of the treatment room (Gantry position 90°, beam direction along arrow) containing the most important elements of the manufacturer representation[51] (shown at gantry position 0°).
Bottom: Horizontal cut at floor level (Gantry position 90°). The four points of fluence-scoring are marked as circles.

III. Results

III.A. Spectra of no room simulation versus full room simulation

In order to evaluate the necessity of a full treatment room model, we first evaluated the USRTRACK simulated neutron spectra per proton treatment Gray in preliminary simulations without any room components. Only the vacuum window, the beam monitor chambers, airgap and phantom were included and compared to the experimental results of Trinkl et al.[37].

It is evident for the exemplary shown 0° and 135° positions of the 200 MeV proton field, that oversimplifying the simulation model by omitting any room components causes mismatches over the whole energy range of the secondary neutrons at both positions (fig. 3).

III.B. Simulated full room model spectra compared to measurements

As a second step, we analyzed the neutron spectra of the full room model and compared these to the measured ERBSS spectra. The neutron spectra for the modeled proton beam therapy scanning nozzle and treatment room for azimuth angles of 0°, 45°, 90° and 135° relative to the beam axis at 2 m distance from isocenter are shown for the $11 \times 11\,\mathrm{cm}^2$ fields at initial beam energies of 200 MeV (Fig. 4), 140 MeV (Fig. 5), 75 MeV (Fig. 7), and 118 MeV with the PMMA range shifter of 5 cm thickness (Fig. 6). The fraction of neutrons from the nozzle in our four phase spaces was < 0.6‰ of all phase space particles. Nearly 100% of secondary neutrons hence originated from the treatment room and phantom.

In general, our results present similar behavior of the neutron spectra inside treatment rooms over the full energy range: a high-energy peak, elevated fluence in the fast neutron region, a approximately $1/E_n$ slope for the epithermal neutrons and a minor peak in the thermal neutron energy range. Depending on proton energy and measurement angle, the relative contributions of these features to the total spectrum differ. The simulated FLUKA neutron spectra display fine resonances which are not present in the ERBSS data, because the ERBSS used response functions with only 130 log-equidistant energy bins and 18 measured

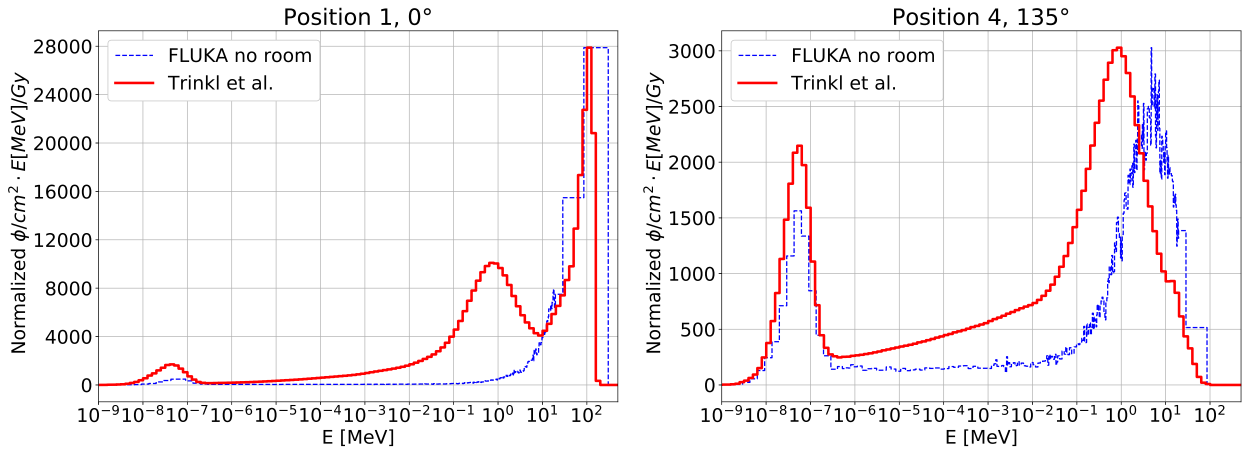

Figure 3: Bare phantom simulation (dashed line) and previously measured data (solid line) in lethargy notation for forward and 135° backscatter direction[37].

count rates to unfold the spectrum in the full energy range, which spanned approx. 11 orders of magnitude.

For FLUKA and Geant4, the laterally integrated depth dose profiles in the PMMA phantom were scored. FLUKA and Geant4 using the FLUKA phase space as input agreed in simulation of the 80% distal falloff range R_{80} of the primary proton beam for all four energies better than 1 mm .

Minor neutron spectra discrepancies between the measured ERBSS and the FLUKA and Geant4 simulations were observed. FLUKA, compared to Geant4 and the ERBSS data, tended to display larger fluence in the high-energy interval for 200 MeV, 0° (Fig. 4 top left) and 140 MeV, 0° (Fig. 5 top left), whereas FLUKA and ERBSS data agreed but were below the measurements for all four proton energies at the 90° off axis position (Fig. 4 - 7 bottom left). Larger discrepancies were present for the 118 MeV, 0° range shifter case for Geant4 (Fig. 6 top left) and the 75 MeV, 135° FLUKA simulation (Fig. 7 bottom right).

Both codes showed reasonably good agreement with experimental data for the four energies and positions by adequately generating the fast neutron shoulder - often called evaporation peak - in the interval 10^{-1} MeV $\leq$ 19.4 MeV. For the whole epithermal interval, the simulations were in close agreement and reflected the spectrum in more detail than the approximately $1/E_n$ slope displayed by the ERBSS data.

Depending on the angle of detector position and beam axis, the relative contributions of the high-energy and evaporation peaks systematically varied. For all four energies, the

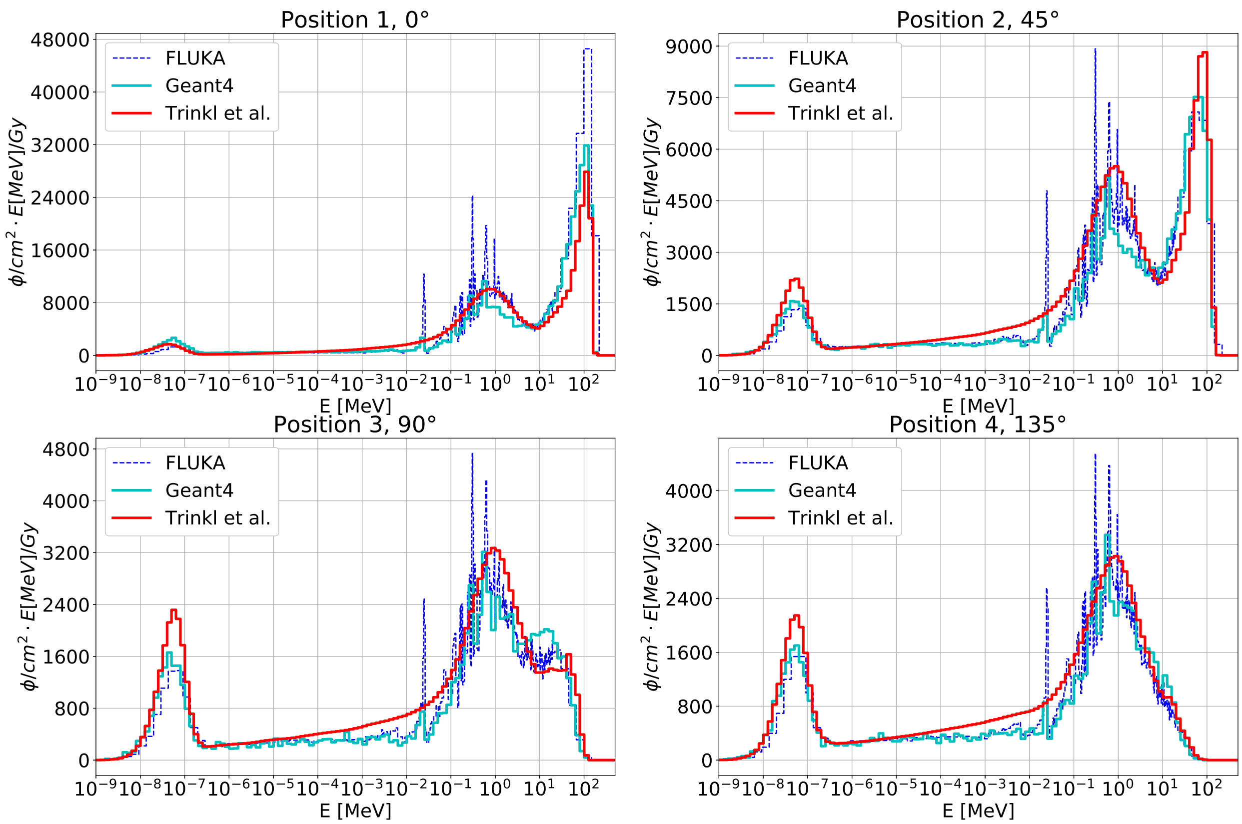

Figure 4: Measured[37] and full-room simulated neutron spectra for the 200 MeV proton field.

high-energy peak (> 19.4 MeV) was more pronounced for smaller observation angles with respect to the beam axis. This finding agrees with the behavior of the spectra reported by Hohmann et al.[31] and Mares et al.[32]. Table 1 displays quantitatively the neutron fraction per energy range. Approximately 50% of neutron fluence for nearly all angles and energies is in the fast neutron range between 10^{-1} MeV and 19.4 MeV. The absolute fluence values per treatment Gray are shown in the most right column of table 1. It is evident that the number of generated secondary neutrons scales with the initial energy of the proton beam. The extreme case is calculated by FLUKA as an increase by a factor of 121 for the 0° measurement position on comparing the proton energies of 75 MeV and 200 MeV (table 1).

III.C. Contribution of room components to neutron energy spectrum

Simulated neutron spectra filtered according to the considered possible neutron sources are here presented exemplarily for the highest beam energy of 200 MeV. The figures for all four proton energies are in the supplementary material[43].

Proton Energy	Position/ Angle	Data source	Fluence ϕ [%] Thermal-n $10^{-9} - 4 \times 10^{-7}$ MeV	Epithermal-n $4 \times 10^{-7} - 10^{-1}$ MeV	Fast-n $10^{-1} - 19.4$ MeV	High-n > 19.4 MeV	Total	Absolute total fluence [$1/(cm^2$ Gy)]
75 MeV	1 / 0°	Trinkl et al.	9.3	21.7	46.4	22.6	100	1772
		Geant4	11.2	18.8	49.3	20.3	100	1845
		FLUKA	5.4	15.7	52.1	26.8	100	1790
	2 / 45°	Trinkl et al.	15.7	20.7	44.9	18.4	100	1507
		Geant4	13.0	19.5	53.0	14.4	100	1453
		FLUKA	10.3	18.0	51.7	19.9	100	1236
	3 / 90°	Trinkl et al.	19.2	25.0	51.7	4.0	100	1210
		Geant4	18.0	26.7	55.1	3.1	100	1211
		FLUKA	15.8	26.2	54.3	3.6	100	910
	4 / 135°	Trinkl et al.	17.2	27.0	55.3	0.6	100	1762
		Geant4	18.8	27.5	53.4	0.3	100	1959
		FLUKA	16.1	28.6	54.7	0.5	100	1266
118 MeV + range shifter	1 / 0°	Trinkl et al.	5.6	20.6	47.1	26.6	100	8926
		Geant4	8.4	18.9	49.8	22.8	100	7260
		FLUKA	3.0	13.3	48.0	35.5	100	9810
	2 / 45°	Trinkl et al.	8.4	18.0	44.1	29.3	100	9210
		Geant4	7.0	14.2	50.2	28.5	100	7721
		FLUKA	6.0	14.9	47.5	31.6	100	7621
	3 / 90°	Trinkl et al.	13.8	26.8	50.4	9.0	100	5106
		Geant4	11.9	20.7	57.8	7.9	100	4628
		FLUKA	11.7	24.0	56.3	7.7	100	4157
	4 / 135°	Trinkl et al.	13.6	28.9	55.3	1.9	100	5712
		Geant4	12.3	27.6	58.3	1.9	100	5192
		FLUKA	12.3	27.6	58.4	1.5	100	4937
140 MeV	1 / 0°	Trinkl et al.	5.0	15.4	42.1	37.4	100	19779
		Geant4	6.3	11.4	37.6	44.6	100	19312
		FLUKA	2.7	9.2	38.3	49.6	100	25421
	2 / 45°	Trinkl et al.	10.8	18.4	43.8	26.8	100	11504
		Geant4	9.7	14.6	46.6	28.9	100	9499
		FLUKA	7.6	15.8	46.6	29.9	100	10583
	3 / 90°	Trinkl et al.	18.0	25.1	49.0	7.8	100	7286
		Geant4	16.9	21.6	54.3	7.1	100	6325
		FLUKA	14.9	24.0	54.0	7.0	100	6371
	4 / 135°	Trinkl et al.	19.2	28.9	49.5	2.3	100	7839
		Geant4	20.8	25.6	52.3	1.1	100	6929
		FLUKA	17.2	28.3	53.2	1.3	100	6691
200 MeV	1 / 0°	Trinkl et al.	4.1	14.3	43.4	38.0	100	83625
		Geant4	5.5	10.1	36.3	48.0	100	86736
		FLUKA	2.2	8.2	36.0	53.5	100	108629
	2 / 45°	Trinkl et al.	9.4	18.4	44.8	27.2	100	43192
		Geant4	9.0	14.0	44.7	32.1	100	34959
		FLUKA	7.2	15.6	46.2	30.9	100	37338
	3 / 90°	Trinkl et al.	17.0	25.3	48.5	9.1	100	24004
		Geant4	16.2	20.6	54.2	8.9	100	19815
		FLUKA	13.6	24.0	53.3	8.9	100	20129
	4 / 135°	Trinkl et al.	18.6	30.2	49.1	2.0	100	21902
		Geant4	18.8	26.1	53.5	1.5	100	18122
		FLUKA	15.9	29.1	53.3	1.6	100	18320

Table 1: Secondary neutron fluence ϕ measured using the ERBSS[37] and that simulated by Geant4 and FLUKA in the present work for the four proton energies at the four detector positions. Data is normalized to the integral neutron fluence in order to compare the fractions.

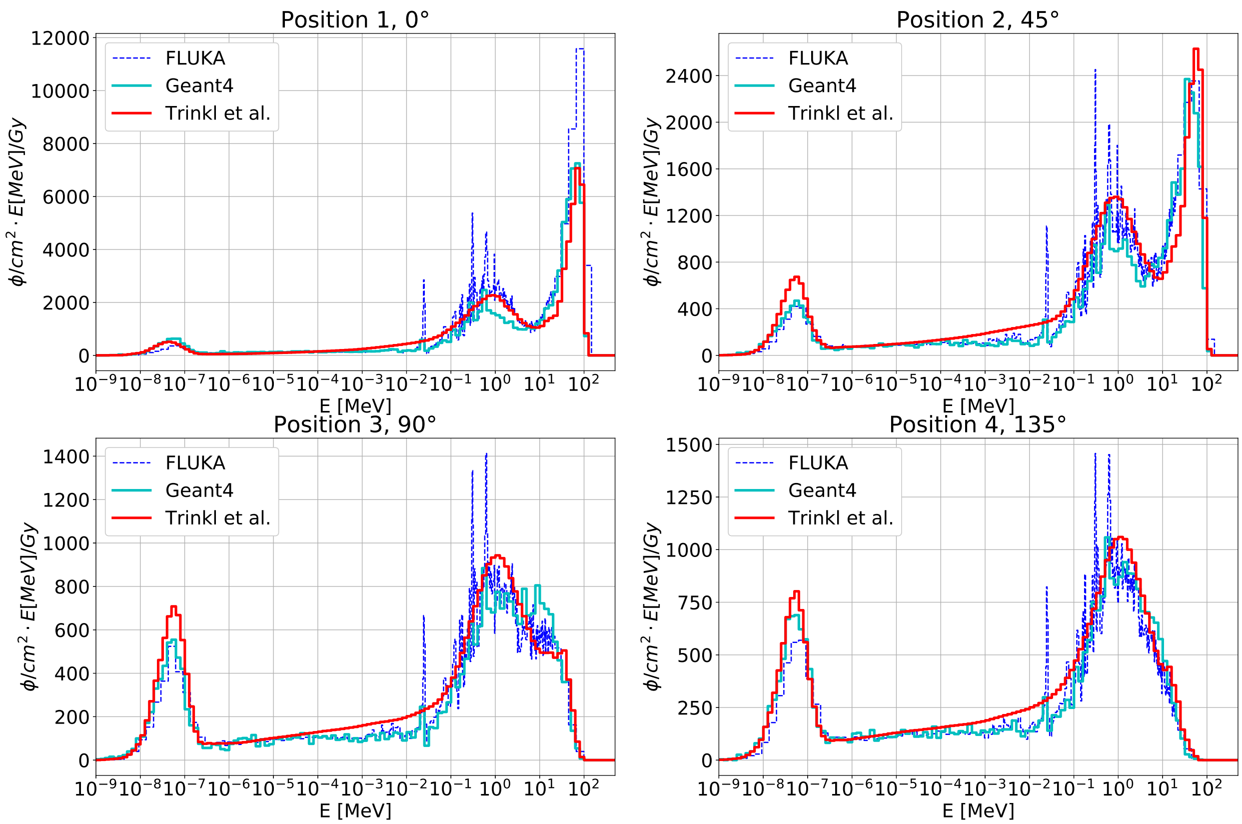

Figure 5: Measured[37] and full-room simulated neutron spectra for the 140 MeV proton field.

The secondary neutron spectra, decomposed by the room elements of production, demonstrate a correlation between energy of the neutron and the room element, especially in the high and fast neutron energy intervals between 10^2 MeV and 10^{-2} MeV.

The high-energy peak at 0° relative to the beam axis (Position 1 in fig. 4) can exclusively be attributed to neutrons from the PMMA phantom (Fig. 8 top). For all four positions, the high-energy region of 10 MeV to 10^2 MeV is governed by phantom-induced neutrons, although the total magnitude is reduced for larger beam angles.

In contrast, the origin of the neutrons in the energy interval 10^{-1} MeV to 10 MeV (cp. fig. 1) is more diverse. For 0° (Fig. 8 top), the two consecutive gantry cylinders modeled as iron are the main source of $\approx$ 70% contributing neutrons. The remaining $\approx$ 30% are shared by counterweight and gantry cone. For the off-axis positions (Figs. 8 bottom, 9 top, 9 bottom), the gantry fraction reduces relative to all remaining room components, which equally contribute. Additionally, as the scoring positions are further off-axis relative to 0°, neutrons originating from the phantom dominate the fast neutron interval.

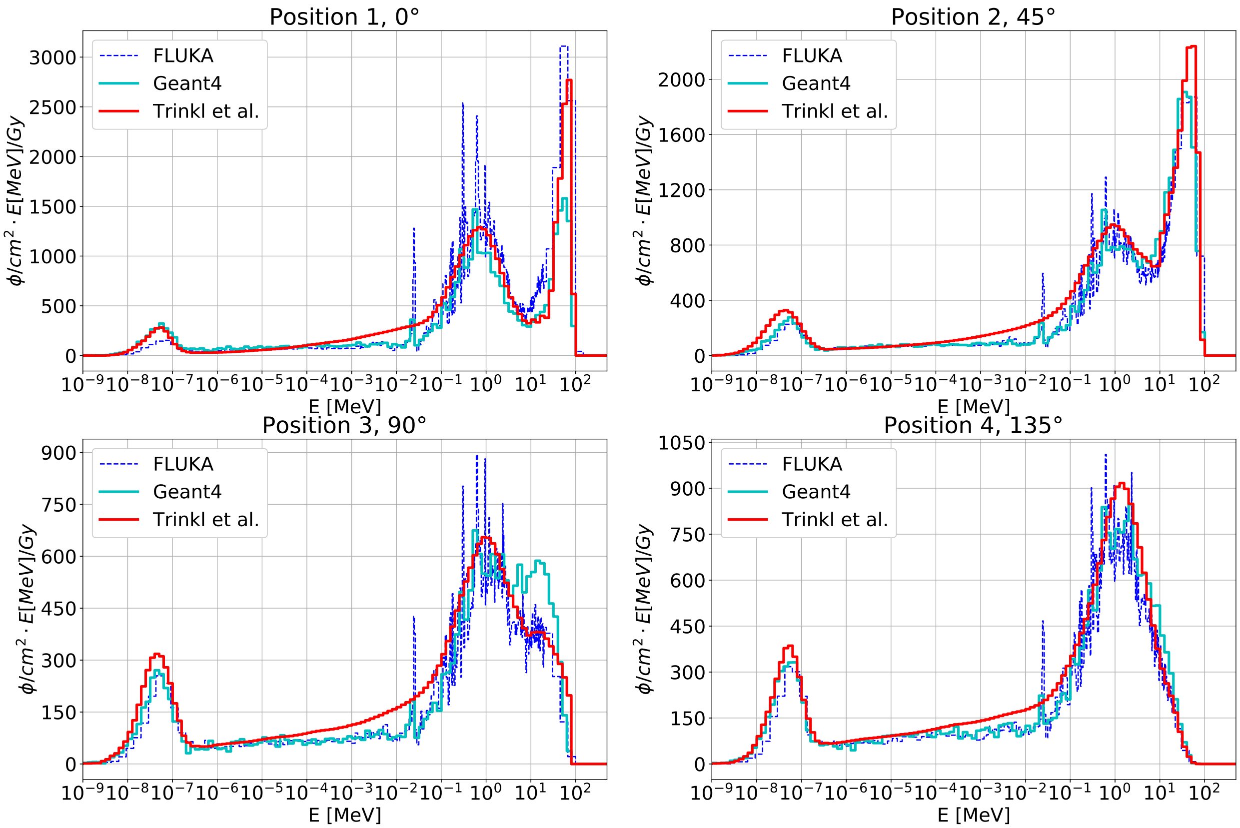

Figure 6: Measured[37] and full-room simulated neutron spectra for the 118 MeV proton field using a PMMA range shifter of 5 cm thickness.

The neutrons in the interval 10^{-8} MeV and 10^{-1} MeV show no distinct room component as a main origin.

The contribution of the secondary neutrons generated within the concrete floor, the iron floor support plate, the bending magnet and the concrete walls individually is more than one order of magnitude lower than the total number generated across all four scorer positions.

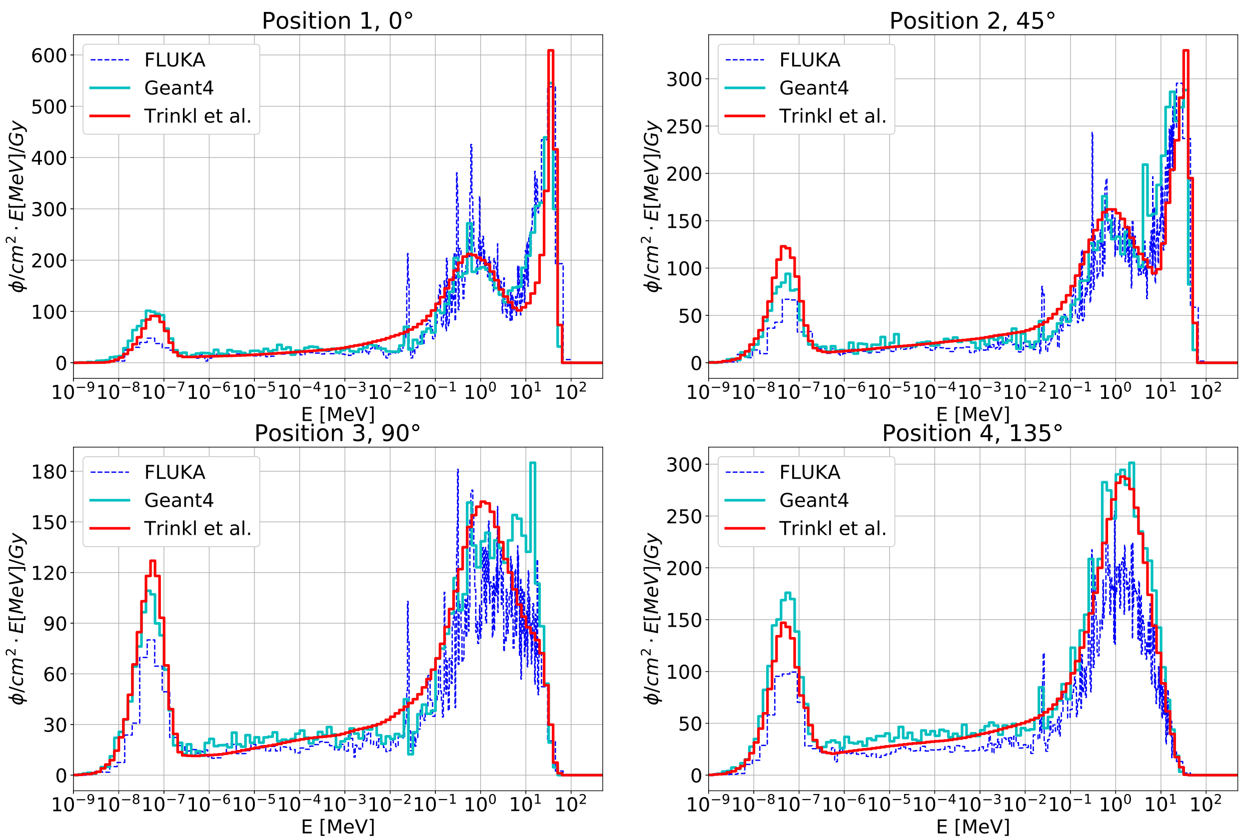

Figure 7: Measured[37] and full-room simulated neutron spectra for the 75 MeV proton field.

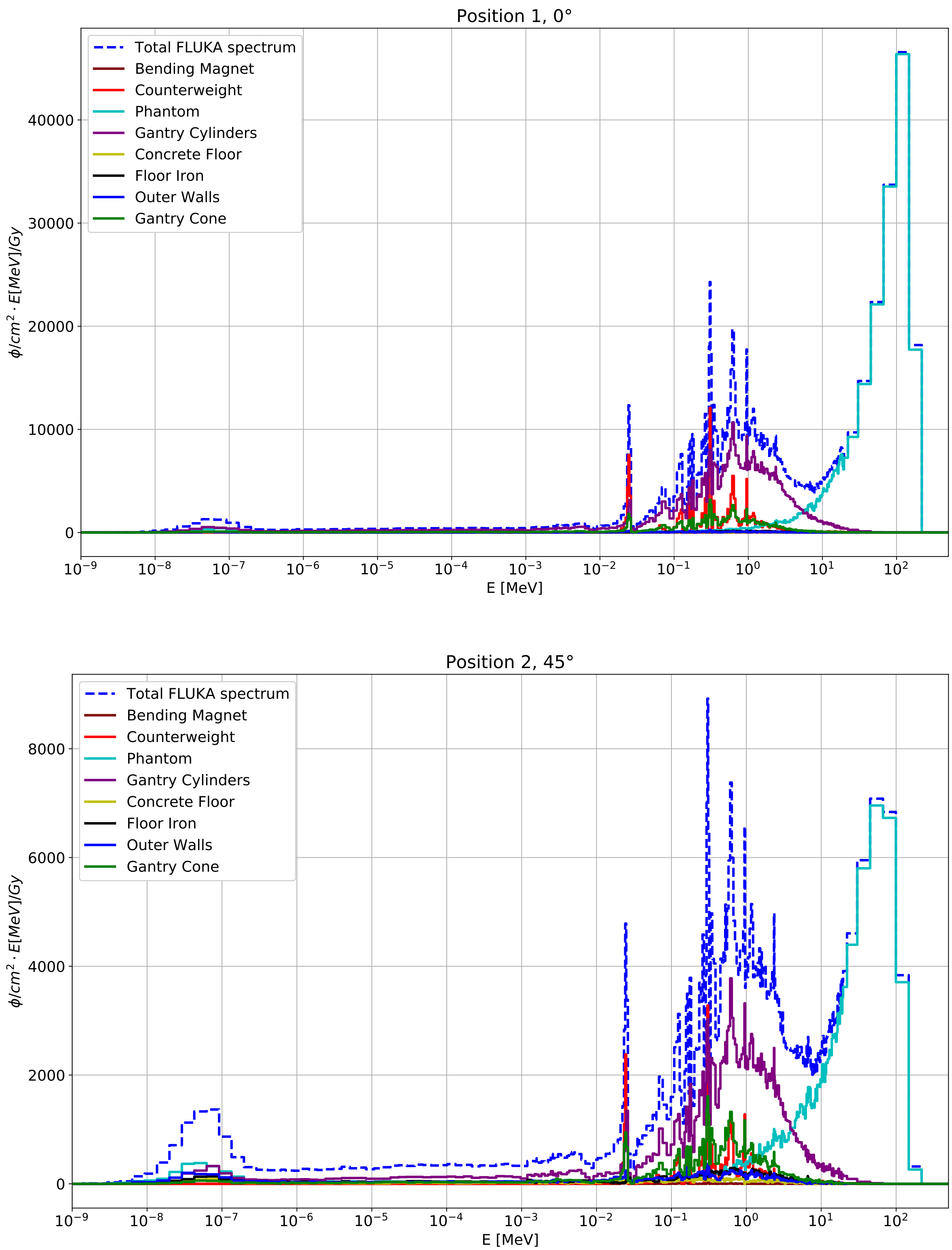

Figure 8: Total neutron spectrum (dashed line) and room component spectra (solid lines) at 0° (top) and 45° (bottom) for the 200 MeV proton field.

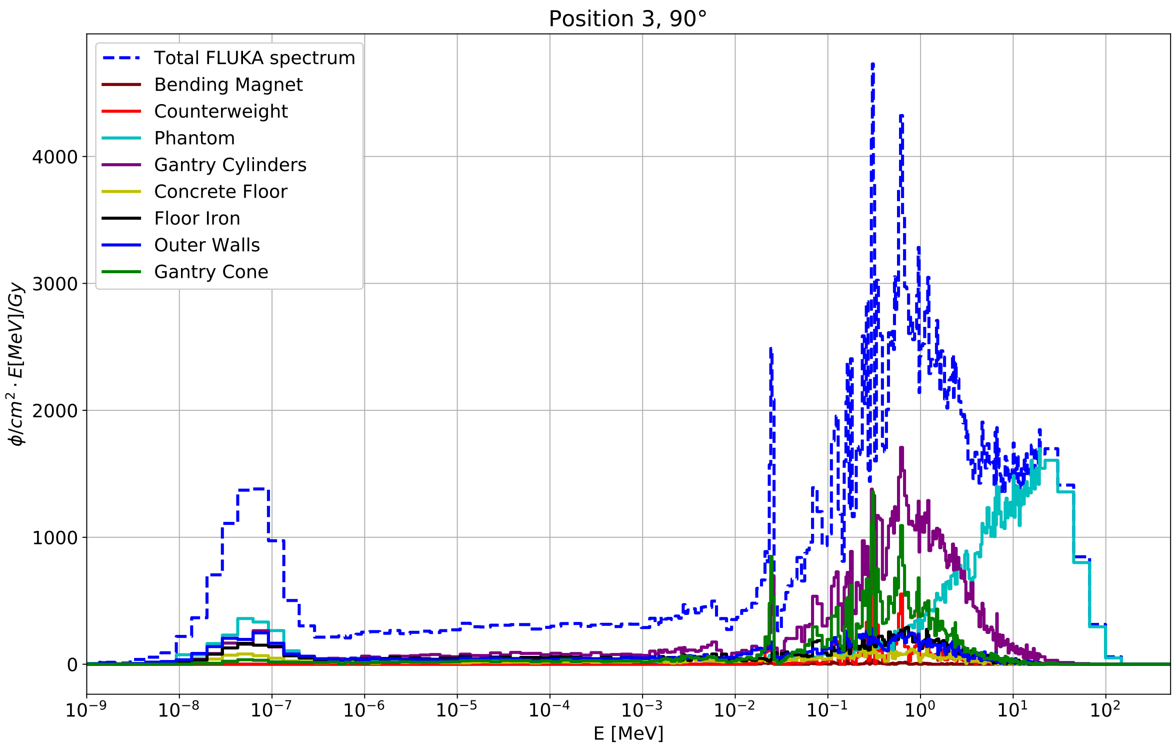

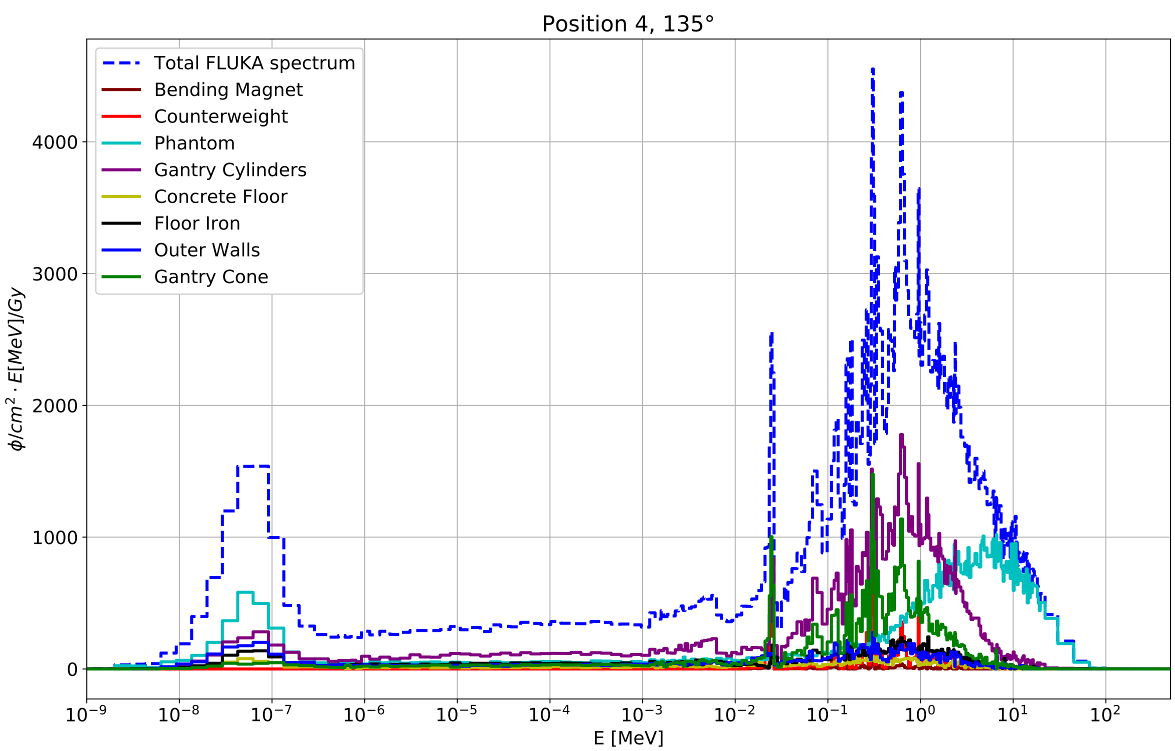

Figure 9: Total neutron spectrum (dashed line) and room component spectra (solid lines) at 90° (top) and 135° (bottom) for the 200 MeV proton field.

IV. Discussion

The measured ERBSS neutron spectra showed the evaporation peak around 1 MeV, i.e. at lower energies compared to the peak simulated spectra without room model, which indicates that the produced secondary neutrons scattered and lost energy inside the treatment room before they reached the detector. We hence modeled the whole room in an attempt to reproduce the measured spectra. Note that for a scattering facility, Sayah et al.[33] reported that the lack of treatment room details in MC simulations can lead to errors in the simulated ambient dose equivalent $H^*(10)$ of up to 45%.

For side and backward directions (90° and 135°) the high-energy peak merges with the evaporation peak. This behavior was already experimentally reported for spot-scanning facilities[37,52]. For all energies and forward angles, the high-energy peak amplitude exceeds the amplitudes of the evaporation and thermal peaks. Especially for the two forward directions (0° and 45°), the relative contributions of the high energy interval can change dramatically, as e.g. from 53.5% for 200 MeV, 0° , to 1.6% for 200 MeV, 135°. The absolute fluence of thermal neutrons is similar within a factor of two for every initial proton beam energy across all four measurement positions. This was explained in the literature as isotropic scattering of the secondary neutrons from the walls[32].

Our results show that the neutrons contributing to the high-energy peak originate predominantly from the phantom itself while the neutrons generated in gantry cylinders and counterweight mainly contribute to the fast (evaporation) peak. A previous ERBSS measurement campaign, although without detailed modeling investigations, already presumed structures of large atomic number (High-Z) materials like iron in forward direction, namely gantry and counterweight to contribute to neutron production in this energy range[32].

At all four measurement positions, the used initial beam energies of 200 MeV, 140 MeV, 118 MeV and 75 MeV show the same magnitude of thermal neutrons (right in tab. 1). As reported previously, these thermalized neutrons originate from high-energy neutrons, which were isotropically scattered multiple times inside the gantry room[32]. Hence, simulations lacking the treatment room failed to reproduce this spectral component (Fig. 3).

Because the neutrons in the energy range 10^{-8} MeV to 10^{-1} MeV show no distinct room component as a main origin, the directionality of the initial emission appears to be lost. In contrast, nuclear reactions in the phantom of type X(p,xn)Y directly generate the high-energy neutrons, which are emitted along the 0° beam axis and directly hit the detector at 0° (Fig. 8 top). Such neutrons interact via a next step in inelastic reactions of Fe(n,xn)Fe with the structures of the counterweight (compared to the bending magnet located in backward direction) and the two gantry wheels, which are located in forward direction and all around the patient table, respectively (Fig. 8 and fig. 9). This finding corroborates the explanations by Mares et al., who, based on ERBSS measurements) claimed that the fast neutron component originates from forward scattered neutrons interacting in the iron-rich counterweight[32]. Furthermore, at the 90° position, there are pronounced contributions in the fast neutron range from the bending magnet, while the contribution from the counterweight is less.

Although the contributions of the secondary neutrons generated within the concrete floor, the iron floor support, the bending magnet and the concrete walls individually are more than one order of magnitude lower than the total signal across all four scorer positions, the walls and massive components cannot be neglected in the model, because the neutrons, when generated in the gantry, are scattered multiple times in these components before reaching the scorer positions. In particular, the thermal peak at energies between 10^{-9} MeV and 4×10^{-7} MeV would be lost in this case.

V. Conclusion

The present study has confirmed a strong dependence of the secondary neutron field on the angle of observation and incident proton beam energy as discussed in recent publications. The comparison of the simulated neutron spectra produced by geometrically well defined, monoenergetic proton fields with measured ERBSS neutron spectra around a homogeneous PMMA phantom have shown that a room model, although simple, is needed to understand the origin of secondary neutrons in general and their energy dependence in particular. The results of this study, which was based on a systematic investigation of production of secondary neutrons from monoenergetic protons at defined geometries, may be generalized in that they can provide a estimation of neutron fields, even at spot-scanning facilities where detailed neutron measurements and simulations cannot be performed. Due to the unavoidable uncertainties from ERBSS measurement unfolding, as well as due to the heterogeneity of nuclear models, used cross-sections and code differences over 13 orders of magnitude of neutron energies between different Monte Carlo codes, a cross comparison of the used codes, FLUKA and Geant4, has been useful.

Identification of the neutron origin has shown that iron-rich room components like the gantry cylinders, the gantry cone and the counterweight contribute most to this energy interval. Of course, massive iron structures are needed for the stability in the whole gantry system, which in turn enables reaching the required sub-mm precision of the proton beam. We propose using Monte Carlo simulations for the design of future pencil beam scanning gentry rooms to investigate options for the reduction of secondary neutrons, although the concept of upright seated proton treatments may be feasible for certain indications without using heavy gantry structures[53]. Such simulations could influence the decisions on gantry construction material or structure, for example on the choice of massive gantry versus a bird cage gantry like structure.

Finally, the presented data can help in including the secondary neutron field in analytical treatment planning systems in order to predict the out-of-field neutron dose to organs far from the treatment field. This is already under investigation for scattering facilities, where a personalized estimate of organ specific neutron equivalent dose may eventually guide medical physicists to create treatment plans which feature reduced risk of late adverse effects[9,54].

Acknowledgement

Franz S Englbrecht acknowledges support from the German research foundation (DFG) Cluster of excellence "Munich Centre for Advanced Photonics (MAP)" (EXC 158, Project number 24819222) and the Munich "Centre for Advanced Laser Applications (CALA)".

Conflict of Interest Statement

The authors have no relevant conflicts of interest to disclose.

References

[1] Allen AM, Pawlicki T, Dong L et al. An evidence based review of proton beam therapy: the report of ASTRO's emerging technology committee. *Radiotherapy and Oncology.* 2012;103(1):8-11.

[2] Mohamad O, Tabuchi T, Nitta Yet al. Risk of subsequent primary cancers after carbon ion radiotherapy, photon radiotherapy, or surgery for localised prostate cancer: a propensity score-weighted, retrospective, cohort study. *Lancet Oncol.* 2019, 5: 674-685.

[3] Newhauser WD, Zhang R. The physics of proton therapy. *Phys. Med. Biol.* 2015;60 R155–R209.

[4] Newhauser WD, Durante M. Assessing the risk of second malignancies after modern radiotherapy. *Nature Reviews Cancer.* 2011; 11(6): 438–448.

[5] Hall EJ. The impact of protons on the incidence of second malignancies in radiotherapy. *Technol Cancer Res Treat.* 2007;6(4 Suppl):31-4.

[6] Schneider U, Hälig A, Baiocco G, Lomax T. Neutrons in proton pencil beam scanning: parametrization of energy, quality factors and RBE. *Phys. Med. Biol.* 2016;61(16):6231-42.

[7] Ottolenghi A. ANDANTE - Multidisciplinary evaluation of the cancer risk from neutrons relative to photons using stem cells and the induction of second malignant neoplasms following pediatric radiation therapy, www.cordis.europa.eu/result/rcn/182088_en.html [Accessed: 10.12.2018]

[8] Hillbrand M, Georg D, Hadner H, Pöttner R, Dieckmann K. Abdominal cancer during early childhood: A dosimetric comparison of proton beams to standard and advanced photon radiotherapy. *Radiotherapy and Oncology.* 2009;89(2):141-9.

[9] Kollitz E, Han H , Kim CH, Kroll C, Riboldi M, Newhauser W, Dedes G, Parodi K. A novel hybrid model for out-of-field dose calculation in proton therapy treatment planning. *Int J Part Ther* 2020;6(4):285.

[10] Rechner L, Eley JG, Howell RM, Zhang R, Mirkovic D and Newhauser WD. Risk-optimized proton therapy to minimize radiogenic second cancers . *Phys. Med. Biol.* 2015;60:3999-4013.

[11] International Commission on Radiological Protection. The 2007 Recommendations of the International Commission on Radiological Protection ICRP 103 www.journals.sagepub.com/doi/pdf/10.1177/ANIB_37_2-4 [Accessed: 10.12.2018]

[12] Zheng Y, Fotenot J, Taddei P, Mirkovic D and Newhauser W. Monte Carlo simulations of neutron spectral fluence, radiation weighting factor and ambient dose equivalent for a passively scattered proton therapy unit *Phys. Med. Biol.* 2008;53:187-201.

[13] Schneider RA, Wisser L, Arnold MR et al. Proton therapy with spot scanning: the Rinecker Proton Therapy Center in Munich. *Nowotwory Journal of Oncology.* 2007;57(5):524-532.

[14] Borchert HJ, Mayr M, Schneider RA et al. Proton therapy with spot scanning: the Rinecker Proton Therapy Center in Munich. Part 2: Technical & physical aspects. *Nowotwory Journal of Oncology.* 2008;58(2):116-124.

[15] Fontenot J, Taddei P, Zheng Y, Mirkovic D, Jordan T, Newhauser W. Equivalent dose and effective dose from stray radiation during passively scattered proton radiotherapy for prostate cancer. *Phys. Med. Biol.* 2008;53(6):1677-88.

[16] Perez-Andajar A, Newhauser WD, DeLuca PM. Neutron production from beam-modifying devices in a modern double scattering proton therapy beam delivery system. *Phys. Med. Biol.* 2009;54(4):993–1008.

[17] Schneider U, Agosteo S, Pedroni E, Besserer J. Secondary neutron dose during proton therapy using spot scanning. *Int J Radiat Oncol Biol Phys.* 2002;53(1):244-51.

[18] Taddei PJ, Fontenot JD, Zheng Y et al. Reducing stray radiation dose to patients receiving passively scattered proton radiotherapy for prostate cancer. *Phys. Med. Biol.* 2008;53(8):2131–2147.

[19] Titt U, Newhauser WD. Neutron shielding calculations in a proton therapy facility based on Monte Carlo simulations and analytical models: criterion for selecting the method of choice. *Radiation Protection Dosimetry.* 2005;115(1-4):144-8.

[20] Farah J, Martinetti F, Sayah R et al. Monte Carlo modeling of proton therapy installations: a global experimental method to validate secondary neutron dose calculations. *Phys. Med. Biol.* 2014;59:2747–2765.

[21] Cywicka-Jakiel T , Stolarczyk L, Swakon J, Olko P, Waligórski MPR. Individual patient shielding for a proton eye therapy facility. *Radiation Measurements.* 2010;45(10):1127-1129.

[22] Tayama R, Handa H, Hayashi K et al. Benchmark calculations of neutron yields and dose equivalent from thick iron target for 52–256 MeV protons. *Nuclear Engineering and Design.* 2002;213(2-3):119-131.

[23] Chen KL, Bloch CD, Hill PM, Klein EE. Evaluation of neutron dose equivalent from the Mevion S250 proton accelerator: measurements and calculations. *Phys. Med. Biol.* 2013;58:8709-8723.

[24] Baradaran-Ghahfarokhi M, Reynoso F, Darafsheh A et al. A Monte Carlo-based analytic model of neutron dose equivalent for a mevion gantry-mounted passively scattered proton system for craniospinal irradiation. *Med. Phys.* 2020;47(9): 4509-4521.

[25] Baradaran-Ghahfarokhi M, Reynoso F, Darafsheh A et al. A Monte Carlo based analytic model of the in-room neutron ambient dose equivalent for a Mevion gantry-mounted passively scattered proton system . *J. Radiol. Prot.*. 2020;40: 980-996.

[26] Howell RM, Burgett EA, Isaacs D et al. Measured Neutron Spectra and Dose Equivalents From a Mevion Single-Room, Passively Scattered Proton System Used for Craniospinal Irradiation. *Int J Radiat Oncol Biol Phys.* 2016;1;95(1): 249-284.

[27] Brenner DJ, Elliston CD, Hall EJ, Paganetti H. Reduction of the secondary neutron dose in passively scattered proton radiotherapy, using an optimized pre-collimator/collimator. *Phys. Med. Biol.* 2009;54(20):6065–6078.

[28] Islam MR, Collums TL, Zheng Y, Monson J, Benton ER. Off-axis dose equivalent due to secondary neutrons from uniform scanning proton beams during proton radiotherapy. *Phys. Med. Biol.* 2013;58(22):8235-51.

[29] Newhauser WD, Titt U, Dexheimer D, Yan X, Nill S. Neutron shielding verification measurements and simulations for a 235-MeV proton therapy center. *Nuclear Instruments and Methods in Physics Research A.* 2002;476:80-84.

[30] Arjomandy B, Sahoo N, Cox J, Lee A, Gillin M. Comparison of surface doses from spot scanning and passively scattered proton therapy beams. *Phys. Med. Biol.* 2009;54(14):N295-302.

[31] Hohmann E, Safai S, Bula Ch et al. Investigation of the neutron stray radiation field produced by irradiating a water phantom with 200-MeV protons. *Nuclear Technology.* 2011;175(1):77-80.

[32] Mares V, Romero-Exposito M, Farah J et al. A comprehensive spectrometry study of a stray neutron radiation field in scanning proton therapy. *Phys. Med. Biol.* 2016;61(11):4127-40.

[33] Sayah R. Evaluations des doses dues aux neutrons secondaires reçues par des patients de différents âges traités par protonthérapie pour des tumeurs intracrâniennes. *Université Paris XI.* 2013

[34] Goebel H. Dose Delivery System Of The Varian Probeam System With Continuous Beam. *Workshop On Innovative Delivery Systems In Particle Therapy.* 2017

[35] Particle therapy facilities under construction www.ptcog.ch/index.php/facilities-under-construction PTCOG Press Releases [Accessed: 11.04.2019]

[36] Zheng Y, Newhauser W, Klein E, Low D. Monte Carlo simulation of the neutron spectral fluence and dose equivalent for use in shielding a proton therapy vault. *Phys. Med. Biol.* 2009;54(22):6943–6957.

[37] Trinkl S, Mares V, Englbrecht F et al. Systematic out-of-field secondary neutron spectrometry and dosimetry in pencil beam scanning proton therapy. *Phys. Med. Biol.* 2017;44(5):1912-1920.

[38] Zheng Y, Newhauser W, Fotenot J, Taddei P, Mohan R. Monte Carlo study of neutron dose equivalent during passive scattering proton therapy. *Phys. Med. Biol.* 2007;52(15):4481-96.

[39] Battistoni G, Cerutti F, Fasso A et al. The FLUKA code: description and benchmarking. *AIP Conference Proceedings.* 2007

[40] Ferrari A, Sala PR, Fasso A, Ranft J, FLUKA: a multi-particle transport code. *CERN-2005-10.* 2005;31-49

[41] Agostinelli S et al. Geant4—a simulation toolkit. *Nuclear Instruments and Methods in Physics Research Section A: Accelerators, Spectrometers, Detectors and Associated Equipment.* 2003;506:250-303.

[42] Langer UW, Eley JG, Dong L, Langen K. Comparison of multi-institutional Varian ProBeam pencil beam scanning proton beam commissioning data. *Radiation Oncology Physics.* 2017;18(3):96-107.

[43] Englbrecht FS, Trinkl S, Mares V et al. Supplemental material for: A Comprehensive Monte-Carlo Study of Out-Of-Field Secondary Neutron Spectra in a Scanned-Beam Proton Therapy Treatment Room. *Zeitschrift für Medizinische Physik Online* 2020.

[44] Boehlen TT, Cerutti F, Chin MPW, et al. The FLUKA code: developments and challenges for high energy and medical applications. *Nuclear Data Sheets.* 2018;120:211-214.

[45] Würl M, Englbrecht FS, Parodi K, Hillbrand M. Dosimetric impact of the low-dose envelope of scanned proton beams at a probeam facility: comparison of measurements with tps and mc calculations. *Phys. Med. Biol.* 2016;61(2):958-73.

[46] Hofmann, W, Dittrich W. Use of isodose rate pictures for the shielding design of a proton therapy centre. *Proc. of shielding aspects of accelerators, targets and irradiation facilities (SATIF 7).* 2004;181-187.

[47] Ferrari A, Sala PR. The physics of high energy reactions. *Nuclear reaction data and nuclear reactors physics, design and safety.* 1997;1-109.

[48] De Smet V et al. Neutron H*(10) inside a proton therapy facility: comparison between Monte Carlo simulations and WENDI-2 measurements. *Radiation Protection Dosimetry.* 2013;161(1-4):417-21.

[49] Avery S, Ainsley C, Maughan R, McDonough J. Analytical shielding calculations for a proton therapy facility. *Radiation Protection Dosimetry.* 2008;131(2):167-79.

[50] The Geant4 Collaboration. Physics Lists EM constructors in Geant4 10.1. 2015

[51] Varian Medical Systems, Inc., Probeam Proton Therapy System www.varian.com/oncology/products/treatment-delivery/probeam-compact-proton-therapy-solution [Accessed: 10.08.2016]

[52] Farah J, Mares V, Romero-Exposito M et al. Measurement of stray radiation within a scanning proton therapy facility: EURADOS WG9 intercomparison exercise of active dosimetry systems. *Medical Physics*. 2015;42(5):2572-84.

[53] Tami Freeman, Upright treatment could increase patient comfort, reduce proton therapy costs, *Physics World* www.physicsworld.com/a/upright-treatment-could-increase-patient-comfort-reduce-proton-therapy-costs [Accessed: 11.10.2020]

[54] Eley J, Newhauser WD, Homann K et al. Implementation of an analytical model for leakage neutron equivalent dose in a proton radiotherapy planning system. *Cancers (Basel)*. 2015;7(1):427-38.